J Mater Sci: Mater Electron (2023) 34:325

Anisotropy of hardness and impression morphology in body-centered tetragonal tin (Sn) at cryogenic temperature and room temperature

Xiaoliang Ji[1,*], Rong An[2], Wei Zhou[1], Yiping Xia[3], Fu Guo[1,4,*], and Chunqing Wang[2,*]

[1] *Faculty of Materials and Manufacturing, Beijing University of Technology, Beijing 100124, China*
[2] *State Key Laboratory of Advanced Welding and Joining, Harbin Institute of Technology, Harbin 150080, China*
[3] *School of Materials Science and Engineering, Harbin Institute of Technology, Harbin 150080, China*
[4] *College of Robotics, Beijing Union University, Beijing 100101, China*

Received: 4 November 2022
Accepted: 3 December 2022
Published online: 31 January 2023

ABSTRACT

Tin (Sn), as the matrix of most lead-free solders, plays a primary role in stress absorption during the service of small-scale solder joints under cryogenic environment. The Sn grain orientation would produce a strong effect on the cryogenic mechanical stability of solder joints due to the anisotropy of Sn with a body-centered tetragonal structure. Here, a clear dependence of grain orientation on the strain-hardening behaviors of Sn at the liquid nitrogen temperature (~ 77 K) was revealed through a convenient and off-line Vickers micro-indentation test within various individual Sn grains. As a comparison, the same micro-indentation tests were also performed at room temperature (~ 293 K). By analyzing the hardness and impression morphology of different indented grains, it is found that Sn grain exhibits a hardening effect with a higher hardness value and a sink-in indentation morphology when the indented crystallographic direction deviates from *c* axis at 77 and 293 K. The tendency to become harder is attributed to reduction in the resolved shear stress on {100}[001] slip system with the deviation, which renders dislocation slip more difficult to be activated. This orientation-dependent hardening effect becomes more pronounced at 77 K because of the occurrence of {301} deformation twinning and the same decrease of resolved shear stress on {301} deformation twinning with the deviation.

Address correspondence to E-mail: jixiaoliang@bjut.edu.cn; guofu@bjut.edu.cn; wangcq@hit.edu.cn

https://doi.org/10.1007/s10854-022-09757-7

1 Introduction

Sn-based lead-free solders have been widely used as the replacements of SnPb solders in the manufacturing of modern green electronics to provide thermal, electrical and mechanical interconnections [1]. The matrix of most lead-free solders is βSn (> 90 wt%) with a structure of body-centered tetragonal (BCT, $a = b = 0.583$ nm and $c = 0.318$ nm) [2], which exhibits a high anisotropy in thermal expansion coefficient [3], elastic modulus [4], atomic diffusion [5], and creep resistance [6]. On the other hand, small-scale lead-free solder joints commonly exhibit morphology of up to a few Sn grains even one Sn grain inside the solder bulk [7, 8]. Therefore, it has been a central topic to reveal the anisotropy of Sn in thermal, electromigration, and creep properties of solder joints at high temperature over these years [5, 6, 9–11].

Recently, deep-space exploration (Mars: 133 K, Moon: 93 K) [12, 13], bioelectronics (77 K or lower) [14], and other extremely cryogenic conditions [15] have driven a demand for electronic devices to reliably work at cryogenic temperatures. This demand has attracted much attention to the cryogenic mechanical stability of Sn-based solders and solder joints. Sn matrix, as the primary stress absorption in solder joints [16], will experience a transition in response to thermally or mechanically induced stress from creep [11, 17] to strain hardening [12] with declining temperature. Extensive work has focused on the anisotropic creep behaviors of BCT Sn at high temperatures [6, 11, 17], which is found to be dominated by diffusion-assisted recovery of dislocation such as climb and cross-slip [11]. However, the anisotropy in strain-hardening behaviors that are controlled by dislocation slip and deformation twinning at cryogenic temperatures [12] remains unclear yet.

On the other hand, it is not facile to fabricate single-crystal Sn solder or solder joint specimens [18] for investigating the anisotropy in cryogenic hardening. But this dilemma can be addressed through micro-/nano-indentation tests that are carried out within individual grains of a polycrystalline specimen [19–21], rendering such tests equivalent to measuring the properties of a single crystal [6]. In addition to directly measured hardness and elastic modulus from indentation tests [22], pile-up or sink-in pattern appearing around imprints is also noteworthy. Displacement of indented materials from the indentation itself leads to pile-up or sink-in pattern [23], which reflects strain-hardening characteristics of indented materials [23–25]. Unfortunately, little attention has been devoted to the suggested strain-hardening information underlying these surface deformation patterns.

In this paper, we built a Vickers micro-indentation system that could perform indentation tests at the liquid nitrogen temperature (LNT, ~ 77 K) and room temperature (RT, ~ 293 K). By virtue of the highly accessible measuring system combined with electron backscattered diffraction (EBSD) and laser confocal microscope (LCM) characterizations, we investigated the hardness and pile-up/sink-in pattern around Vickers impressions on different indented grains and then revealed the dependence of indented direction on strain-hardening behaviors at LNT and RT as a comparison.

2 Experiments

Considering the difficulty to carry out the nano-indentation test at LNT because of the effect of thermal drift, the indentation experiments at LNT used a more cost-effective and accessible Vickers indentation system, which was equipped with a custom-built cooling trough to hold liquid nitrogen (LN2) (Fig. 1a) [26]. As a comparison, the same indentation tests were also carried out at RT. Considering the hardening effect of Sn at cryogenic temperatures, the LNT-indentation peak load within individual Sn grain was set to 0.98 N (100 gf), larger than the peak load at RT (0.245 N, 25 gf). The dwell time at the peak load in all experiments was 10 s. The dwell time was much shorter than the period of conventional indentation creep tests at RT (1800 s or longer) [6]. Therefore, the Vickers micro-indentation tests performed here corresponded to initial inelastic deformation stage at RT instead of creep.

A square grid of Vickers indents with a nominal spacing of 150 μm was made on the as-annealed Sn plates with grain size in the sub-mm range (Fig. 1b–c). For LNT-indentations, Sn specimens were firstly put inside the trough and then submerged by the poured liquid nitrogen for 30 min to ensure that indents were performed at LNT [26]. Before indentation experiments, Sn plates were polished to observe the surface morphology changes induced by Vickers indentation.

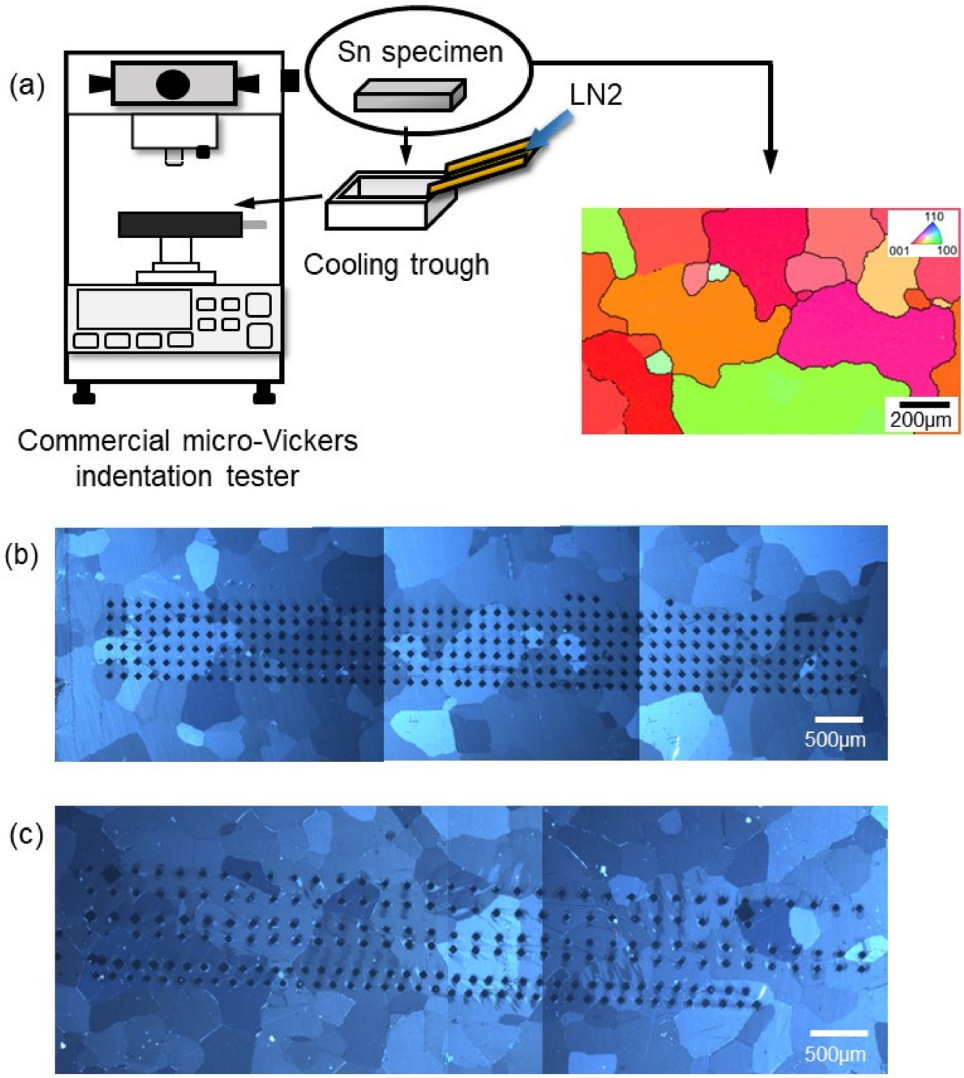

Fig. 1 **a** Set-up of micro-Vickers indentation experiments performed at LNT and RT with EBSD ND-IPF of Sn specimens used. Polarization microscope images of the rectangle grid of Vickers indents made at RT (**b**) and LNT (**c**)

After indentation experiments, all indents were scanned with LCM (OLS5000, Olympus) to record their surface topographical features. The morphology of indents was examined by a scanning electron microscope (SEM, JXA-8230, JEOL) to investigate the indentation-induced surface morphology changes. Afterwards, we selected those indents located inside single Sn grain to carry out further analysis. The crystallographic orientations of grain under those chosen indents were identified as Euler angle (φ_1, Φ, φ_2) using the EBSD technique (EDAX OIM 6.0) in a SEM (Quanta 200 FEG, FEI). The Φ angle represents declination angle between normal direction (ND) of the sample stage and *c* axis of the indented BCT Sn grain [27]. Herein, the indented direction (perpendicular to sample surface) was set to parallel to ND of the sample stage. Figure 1 displays ND-inverse pole figure (ND-IPF) of as-annealed Sn specimens.

3 Results and discussion

3.1 Dependence of Vickers hardness on indented direction

Figure 2 illustrates RT- and LNT- Vickers hardness when the indenter was penetrated into the Sn grain at different declination angles (Φ) with its *c* axis. The RT hardness results shown in Fig. 2a demonstrate a dependence on the indented crystallographic direction. The Sn grains with a declination angle close to 0° have the lowest hardness of ~ 6 MPa. As the

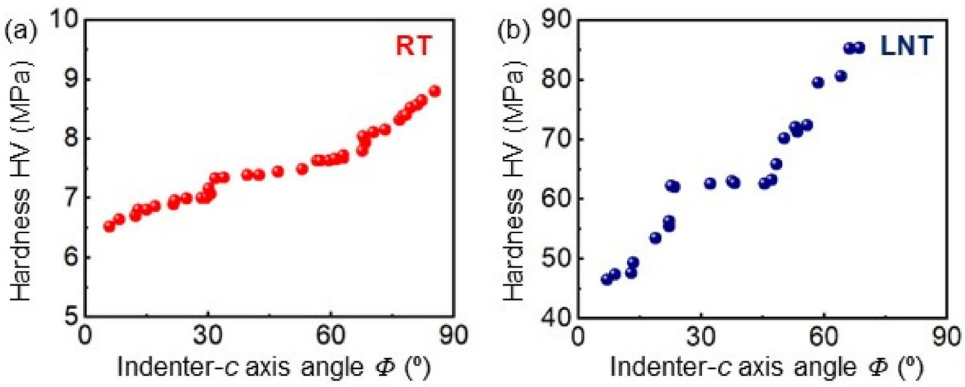

Fig. 2 Relationship of RT- (**a**) and LNT- (**b**) Vickers hardness with the declination angle of indenter from *c* axis

indented direction gradually deviates from *c* axis, the RT hardness of βSn grain exhibits a slight increase. The hardness of indented grains with a deviation angle close to 90° reaches ~ 9 MPa. On the other hand, the LNT hardness of βSn grains increases considerably compared to the RT results, as revealed in Fig. 1b. For example, there is a nearly six times enhancement when the indenter was both pressed along *c* axis at RT and LNT. The LNT hardness results exhibit a similar but stronger indented direction dependence. The grains also have the lowest LNT hardness of ~ 45 MPa when the indenter enters along the *c* axis, while the hardness value exhibits a huge increase with the deviation of indentation axis. The LNT hardness of βSn grains already increases to ~ 85 MPa at a Φ angle of ~ 66°. Due to the cryogenic hardening of Sn, the LNT hardness values are much larger than their RT counterparts. Moreover, the hardness anisotropy depending on the declination angle between indented crystallographic direction and *c* axis becomes stronger with the declining temperature.

3.2 Indented direction dependence of impression morphology

It is generally known that the determination of hardness depends on the value of the contact area between the indenter and the specimen [26]. In Sect. 3.1, the area (A) is obtained from the average length of diagonals ($\bar{d}$) according to Eq. (1)

$$A = \frac{\left(\frac{\bar{d}}{\sqrt{2}}\right)^2}{\sin\frac{\alpha}{2}} \quad (1)$$

where α is the angle between two opposite faces of the diamond Vickers indenter (136°). However, the Eq. 1 ignores the influence of surface deformation around Vickers imprints including pile-up and sink-in [22, 28]. Figure 3a reveals that the true contact area (solid lines) between the indenter and the specimen appears to be smaller than the calculated area (dashed lines) from diagonal length when sink-in predominates, while it becomes larger than the latter in the event of pile-up [23–25]. It is found that not taking the surface deformation pattern into account will introduce significant errors of up to 60% in the contact area [25], meaning that the Vickers hardness displayed in Sect. 3.1 can only be referred to as a

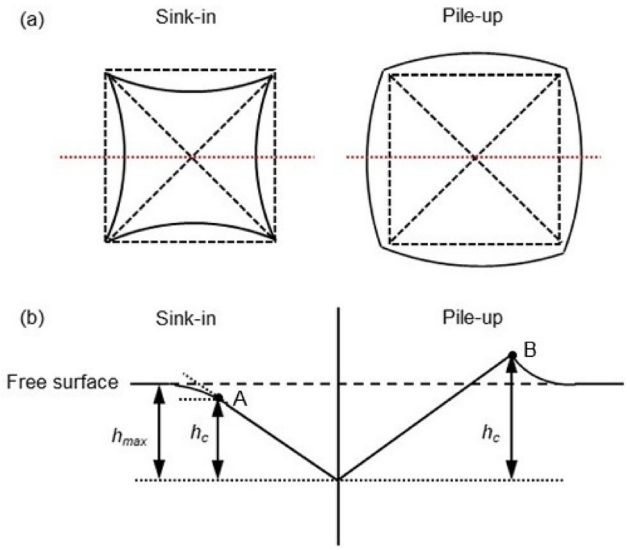

Fig. 3 **a** Schematic illustrations of sink-in and pile-up morphology around the true contact periphery of a Vickers indentation indicated by solid lines while dashed lines represent the nominal contact periphery determined by diagonals of indentation, **b** Height profile along mid-sides of the impression (red dotted line in (a))

nominal hardness. In order to reveal a more accurate anisotropy in hardening behavior for BCT Sn, hence, we compare the surface topographical features around the indentations with a different Φ angle between indenter and c axis and quantitatively characterize the surface deformation patterns of pile-up or sink-in.

Figures 4 and 5 display SEM and 3D LCM topographical morphology with height profiles of RT- and LNT- indents at different Φ angles, respectively. At RT, the imprint on the grain with $\Phi = 13^\circ$ displays the development of pile-up with obvious bulges at the imprint sides. However, a sink-in pattern denoted by a pincushion shape occurs on the grain with a Φ angle of 80°. At LNT (Fig. 5), the SEM morphology and LCM height profiles of indented grain with $\Phi = 9^\circ$ show that sink-in occurs near the impression followed by pile-up; while the impression on the grain with a Φ angle of 46° displays an obvious sink-in pattern without the following pile-up. Hence, it is evident that both the shape of Vickers indents and surrounding surface deformation patterns also depend on the deviation angle of indenter from c axis. Moreover, it is noteworthy that there were not any brittle cracks seen around the Vickers indentations at LNT, which is different from the brittle fracture occurring during LNT uniaxial tensile experiments of Sn [12]. The embrittlement difference should be attributed to the different stress state for Vickers indentation and uniaxial tensile experiments. According to strength theory of metallic materials [29], the tendency towards brittle fracture under certain stress state could be determined by the stress softening coefficient α. The α is defined as the ratio between maximum shear stress (τ_{max}) and maximum homogeneous stress (S_{max}), i.e., Equation (2).

$$\alpha = \frac{\tau_{max}}{S_{max}}$$
$$\tau_{max} = \frac{\sigma_1 - \sigma_3}{2}$$
$$S_{max} = \sigma_1 - v(\sigma_2 + \sigma_3) \quad (2)$$

in which σ_1, σ_2, σ_3 are the principle stress applied on Sn specimens under loading and v is the Poisson's ratio. Accordingly, when the value of α is higher than 1, it is easy for the Sn specimens to carry a large plastic deformation, and the higher the value of α

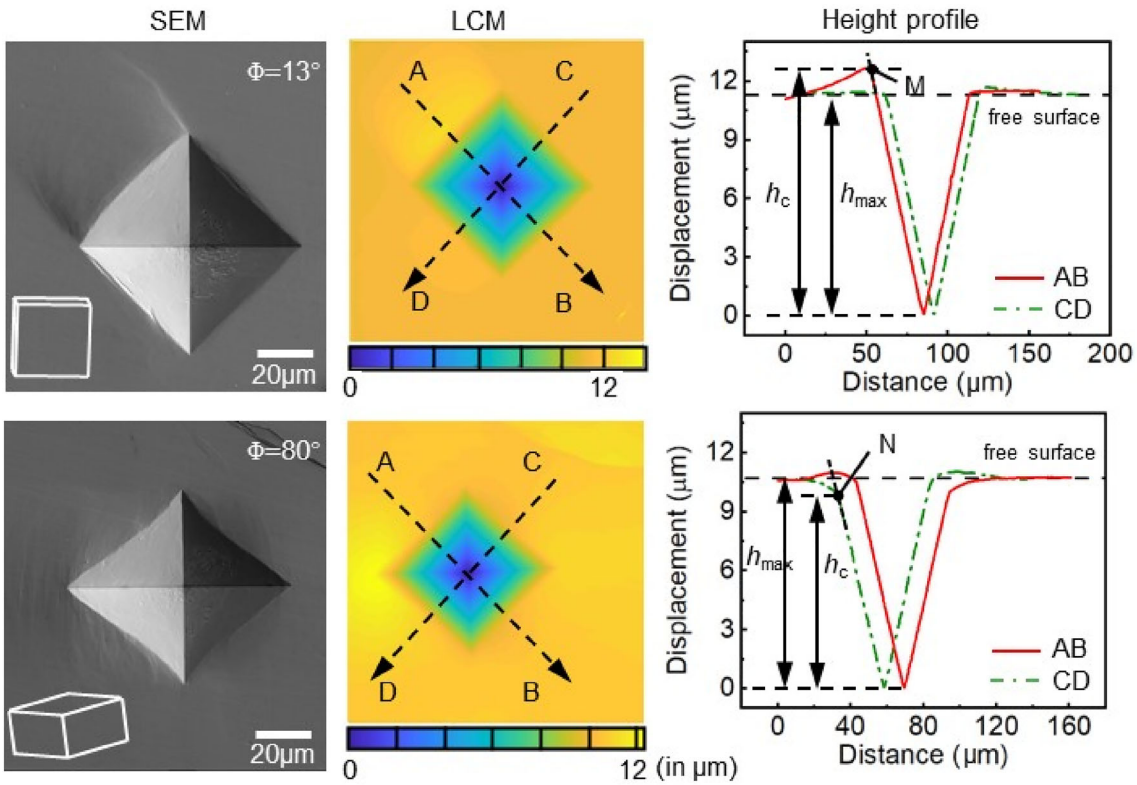

Fig. 4 SEM morphology and LCM topography maps of RT-indents within two individual Sn grains performed at different Φ angles with height profiles along the mid-sides of the impressions

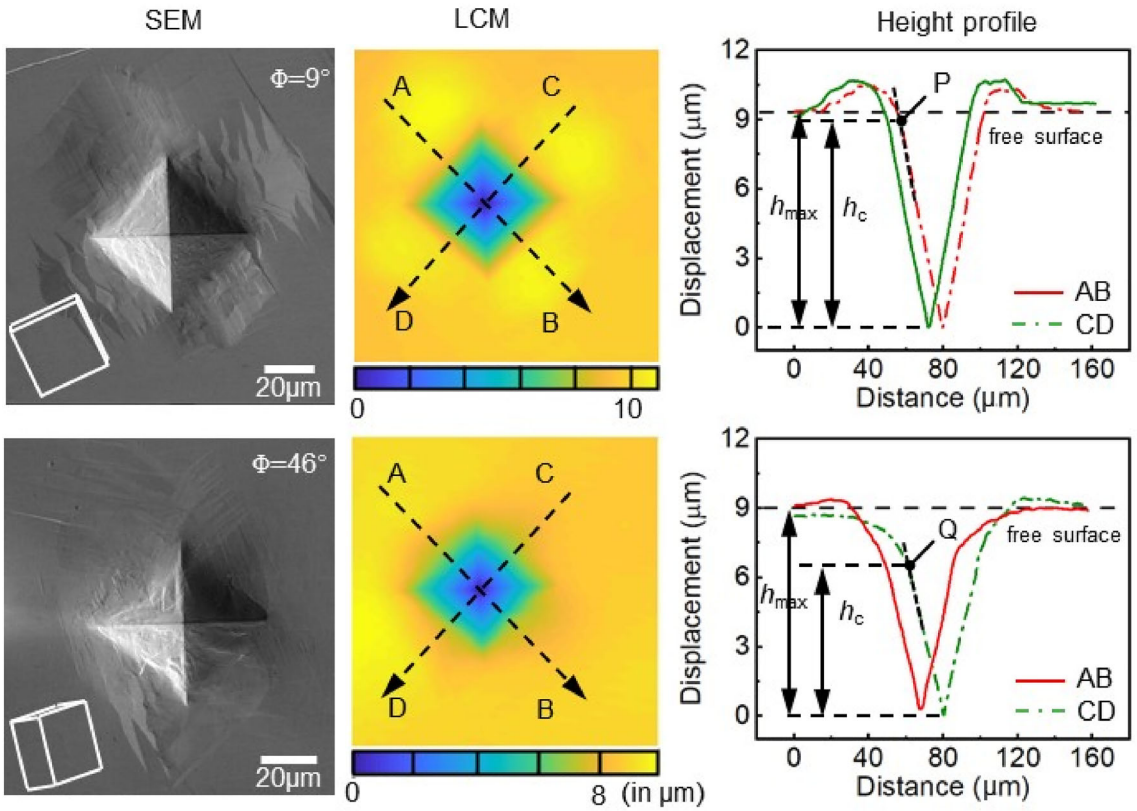

Fig. 5 SEM morphology and LCM topography maps of LNT-indents within two individual Sn grains performed at different Φ angles with height profiles along the mid-sides of the impressions

appears, the easier the occurrence of plastic deformation is. On the other hand, when α is lower than 1, the tendency to brittle fracture becomes increased, and the smaller the α is, the easier the occurrence of brittle fracture is. For uniaxial tensile experiments (uniaxial tension stress), the α is 0.5; while it increases to 4 for the Vickers indentation experiments (triaxial unequal compression stress). Hence, although both the uniaxial tensile experiments and the Vickers indentation were carried out at LNT, brittle fracture occurred under the former loading state while brittle cracks were not present around the Vickers indents.

In order to quantitatively characterize this orientation dependence, we calculate the degree of surface deformation (A_{sd}) around the Vickers impression, which is defined as h_c-h_{max}/h_{max}[25]. As shown in Fig. 3b, the values of h_{max} and h_c are acquired from the height profiles along mid-sides of the indentation upon complete unloading. h_{max} denotes the maximum penetration depth underneath the free surface, and h_c sets the location of the true contact perimeter [25, 30]. In this paper, h_c is determined to be the vertical distance from the bottom center of imprint to a deflection point (e.g., Points A and B in Fig. 3b, M and N in Fig. 4, as well as P and Q in Fig. 5) [30], where the curvature of profile trace changes abruptly. It means that these points can be obtained by calculating the slope of mid-line height profiles with the line distance, as shown in Fig. S1. Thus, $A_{sd} > 0$, indicates pile-up, whereas $A_{sd} < 0$ corresponds to sink-in. Moreover, the higher the positive A_{sd} is, the larger the degree of pile-up appears, while a lower negative A_{sd} corresponds to a severer sink-in pattern around the imprint. As shown in Figs. 4 and 5, there is a value of A_{sd} for each side of the Vickers impression and the average value ($\overline{A_{sd}}^{i}$) is determined as the measure of surface deformation around the i^{th} indentation in one indented Sn grain. Accordingly, the average value of $\overline{A_{sd}}^{i}$ ($i \geqslant 3$) in one indented Sn grain ($\overline{A_{sd}}$) could be referred to as the given surface deformation degree when one Vickers indentation is produced under the same load and temperature on the grain.

Figure 6 demonstrates computed results of $\overline{A_{sd}}$ for RT- (Fig. 6a) and LNT- (Fig. 6b) indented Sn grains at

different declination angles with *c* axis. At RT, when the indented direction is closely parallel to *c* axis of BCT Sn grain (Φ close to 0°), the largest pile-up occurs around the indentation. As the indented crystallographic direction gradually deviates from *c* axis, the pile-up degree gradually decreases and a sink-in pattern therefore appears around the indentation. On the other hand, the LNT-indentations exhibit a surface deformation pattern of sink-in. With the increase of declination angle between the indented crystallographic direction and *c* axis, the extent of sink-in pattern increases significantly, as revealed in Fig. 6b.

Additionally, it is well known that surface deformation patterns occurring around one indentation are strongly dependent on the strain-hardening potential of the indented material [23]. As illustrated in Fig. 7a, as the Vickers indenter is penetrated into one Sn grain with a high strain-hardening potential, the early contact region of the indented grain with the indenter becomes strain hardened so that it is difficult to produce further displacement in this region. With downward penetration of the indenter, the Sn grain needs to displace laterally to accommodate the increasing diameter of indenter. Compared to the strain-hardened region (red region), it is easier to displace the adjacent region which lies deeper below the indenter. Consequently, the deeper Sn flows out laterally. Once this region also strain hardens, further lateral displacement will occur at a still greater depth. As a result, the material around the indentation is left at a lower level than the material farther away from the indenter, producing a sink-in pattern. By contrast, when one Sn grain with a low strain-hardening potential is displaced by penetration of the Vickers indenter (Fig. 7b), the early displaced region does not produce such obvious strain hardening that both the upper and the deeper materials move laterally with descending of the indenter. Thus, the material around the edge of the indentation is raised above the free surface and a pile-up pattern appears. In one word, sink-in and pile-up occur in the indented Sn grain showing high and low strain-hardening potential, respectively. Combined with the orientation dependence of pile-up/sink-in extent around the indentation revealed in Fig. 6, it can be concluded that Sn grain appears softest when the Vickers indenter is penetrated along the *c* axis while it becomes harder with the deviation of indenter from *c* axis. This suggested orientation-dependent hardening information underlying the pile-up/sink-in pattern around indentations is consistent with the hardness anisotropy of Sn grain revealed in Fig. 2. Hence, both the hardness measurement without considering surface deformation around imprints (Fig. 2) and the quantitative characterization of surface deformation patterns (Fig. 6) suggest that Sn exhibits hardening behavior with the deviation of indented direction from *c* axis at LNT and RT.

3.3 Analysis of dislocation slip activated under the indentation load

It is generally known that BCT Sn has a high anisotropy in mechanical properties at both high and cryogenic temperatures. As displayed in Figs. 2 and 6, Sn appears hardening when the indented direction of Vickers indenter deviates from *c* axis and this hardening phenomenon becomes more prominent at LNT. The orientation-dependent hardening can be qualitatively correlated with the resolved shear stresses for dislocations on slip systems estimated from Schmid's law for uniaxial compression [19, 31]. Furthermore, when dislocations glide out of the free

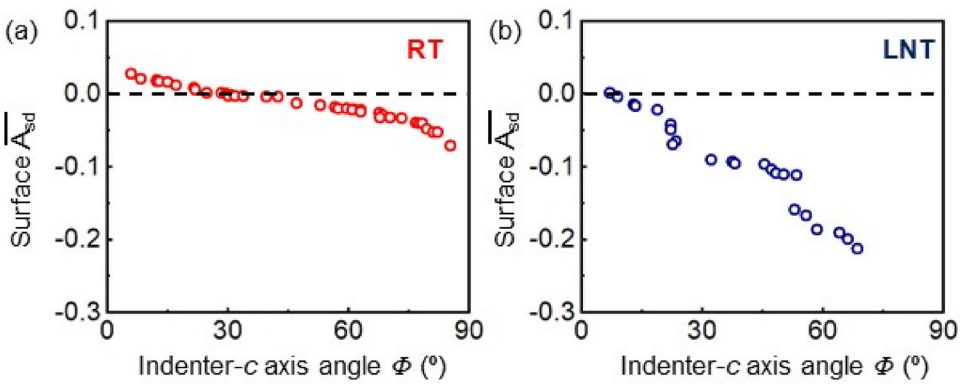

Fig. 6 Relationship of the average $\overline{A_{sd}}$ around RT- (**a**) and LNT- (**b**) Vickers indentations with the declination angle of indenter from *c* axis

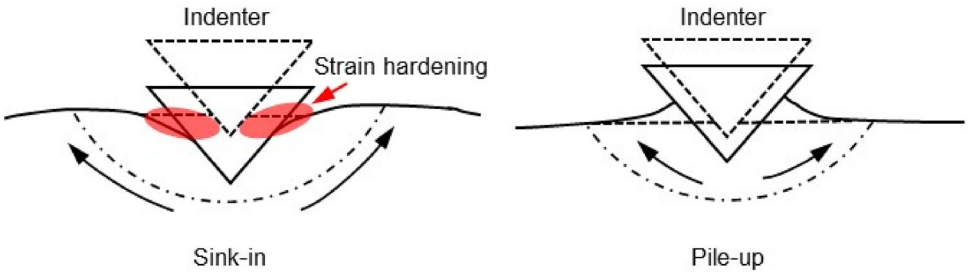

Fig. 7 Schematic illustrations showing the dependence of strain hardening on the indentation morphology

surface, deformation ledges will be left on the surface plane. These ledges will appear along the line direction which corresponds to the intersection of the dislocation slip plane and the surface plane [4, 32]. Therefore, the activated slip plane can be determined through matching these surface ledges in SEM with plane traces of the common slip planes in BCT Sn according to the "trace analysis" in EBSD analysis software (OIM 8.6).

As shown in Figs. 8 and 9, the surface deformation ledges occurring around the representative RT- (Fig. 4) and LNT-indentations (Fig. 5) on the initially polished surface correspond exactly to the (100) plane. Moreover, since Peierls-Nabarro stress (τ_{P-N}) has an inverse exponential relationship with the interplanar distance (d) of slip plane (Eq. 3) [33, 34],

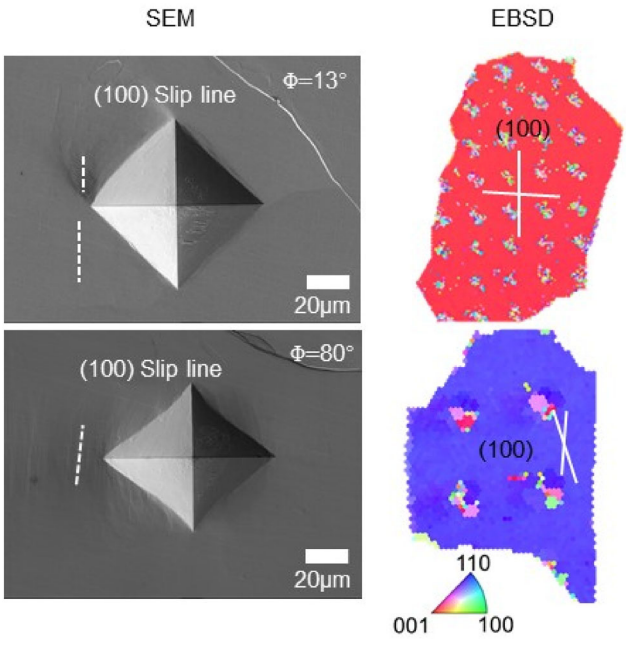

Fig. 8 SEM characterization of deformation ledges appearing around the RT-indents shown in Fig. 4 and corresponding EBSD (100) plane trace analysis determine the activation of (100) slip system under the RT indentation load

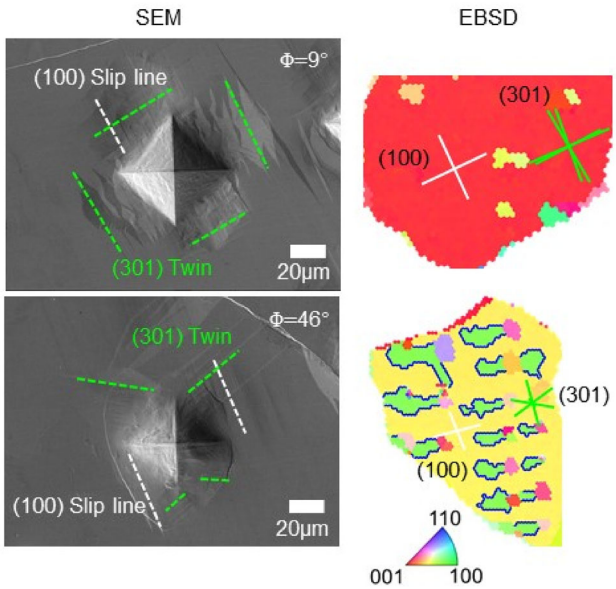

Fig. 9 SEM characterization of deformation ledges appearing around the LNT-indents shown in Fig. 5 and corresponding EBSD (100) plane trace analysis determine the activation of (100) slip system under the LNT-indentation load

$$\tau_{P-N} = \frac{2G}{1-\nu} \exp\left[-\frac{2\pi d}{(1-\nu)b}\right] \quad (3)$$

dislocation slip on {100} planes, which are the closest-packed planes in BCT Sn with the maximum interplanar distance (d = 0.5831 nm), would be easiest to be activated. Hence, the primarily activated slip plane can be determined to be {100} plane under the indentation load. With respect to slip direction on the {100} slip plane, there are [001], $< 010 >$ and $< 011 >$ crystallographic directions for BCT Sn [35, 36]. According to Eq. 3, the smaller the atomic distance in the slip direction (b) is, the smaller the τ_{P-N} in the slip direction would be. On comparing the atomic distance (b) in the three directions, it is found that the value of b in [001] direction is the lowest (0.3182 nm), while the value of b in $< 010 >$ and $< 011 >$ direction is 0.5831 and

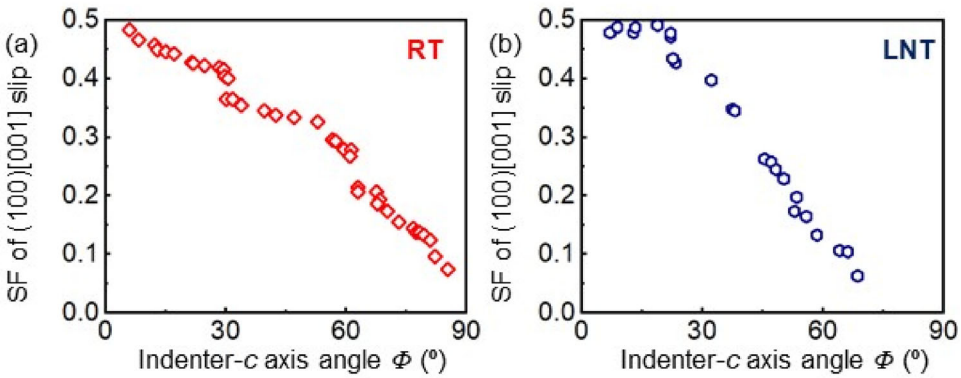

Fig. 10 Maximum Schmid factor (m) for {100}[001] slip systems at different declination angles Vickers indenter with c axis of Sn grains. **a** RT, **b** LNT.

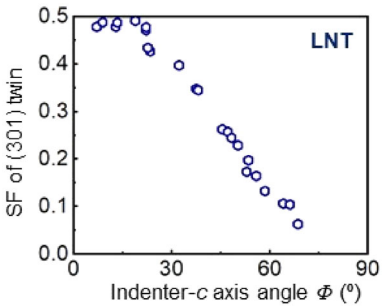

Fig. 11 Maximum Schmid factor (m) for {301} deformation twinning at different declination angles of LNT Vickers indenter with c axis of Sn grains

0.6643 nm, respectively. Hence, the τ_{P-N} in [001] direction on {100} slip plane should be the lowest. In other words, the ease of continuous activation of {100}[001] slip systems, which is determined by the resolved shear stress, should play an important role in the orientation-dependent hardening behavior occurring in BCT Sn at LNT and RT.

According to the Schmid's law, the resolved shear stress on {100}[001] slip systems is proportional to the Schmid factor (m) [31]. Figure 10 reveals the dependence of m value on the declination angle between indented direction and c axis at RT and LNT. It can be found that the grains have the largest value of m ($\sim$ 0.5) for {100}[001] slip systems when Φ angle is close to 0°; while the value of m decreases with deviation of the indented direction from c axis. The reduction in m with the deviation indicates that the corresponding resolved shear stress also decreases; the activation of dislocation slip on {100}[001] therefore becomes more difficult. As a result, Sn grain becomes harder when the Vickers indenter is penetrated at a larger Φ angle with the c axis.

3.4 {301} Deformation twinning occurring at LNT

Apart from dislocation slip on {100}[001] slip systems, there are deformation twins to be activated under the indentation load at LNT because other ledges around the LNT-indents on the initially polished surface are found to correlate with {301} twin planes (Fig. 9). These {301} deformation twins prevent movement of dislocations [12] and thus produce a significant hardening effect in the part of indented grain that is displaced early. Consequently, it becomes difficult to displace this harden part while easier to displace the adjacent materials that lies deeper below the harden part when the Vickers indenter is penetrated continuously. Eventually, all the LNT-indents are pincushion-shaped and demonstrate a sink-in pattern, as shown in Fig. 5 and Fig. S2. More importantly, the ease of activation of {301}<10 − 3 > twinning systems also depends on the resolved shear stress (Schmid factor, m) according to Schmid's law [37, 38]. Figure 11 reveals the relationship between the maximum m for four {301}<10 − 3 > twinning systems in BCT Sn and the indenter-c axis angle at LNT. Similarly, the value of Schmid factor (m) for {301} deformation twinning also decreases when the LNT indented direction deviates from c axis, indicating the reduction of corresponding resolved shear stress for deformation twinning. The activation of {301} deformation twinning therefore becomes more difficult with deviation of indented crystallographic direction from c axis of BCT Sn. Thus, there exist a more considerable difference in the Vickers hardness and surface deformation degree around imprints when the Vickers indenter is penetrated at a larger declination angle with the c axis at LNT.

4 Conclusion

In this paper, systematic micro-Vickers indentation tests at RT and LNT, together with characterization about indentation-induced surface morphology changes using LCM and SEM, were carried out within various individual Sn grains with different crystallographic orientations. The following central conclusions can be drawn:

1. BCT Sn becomes harder, indicated by a higher hardness value and a sink-in indentation morphology, when the indented crystallographic direction deviates from its *c* axis.
2. The activated slip system in BCT Sn grains is determined to be {100}[001] under the Vickers indentation load at LNT and RT. Apart from dislocation slip, {301} deformation twinning is also activated in BCT Sn under the loading of Vickers indenter at LNT.
3. Based upon the dependence of Schmid factor (m) for {100}[001] slip systems on the indenter-*c* axis angle, such hardening behavior of BCT Sn can be attributed to the reduction of resolved shear stress on the slip system with this deviation. Additionally, due to the decreasing Schmid factor (m) for $\{301\}\langle 10-3\rangle$ twinning system with this deviation and the impeding effect of {301} deformation twins on dislocation glide, BCT Sn exhibits stronger grain orientation hardening behavior at LNT and becomes harder compared with the RT counterparts.

Acknowledgements

This work was supported by the Project funded by China Postdoctoral Science Foundation (2022M710271) and the National Natural Science Foundation of China (No. U1537207, No. 61904008). The authors would like to thank the financial support from Innovative Research Group Project of National Natural Science Foundation of China (51621003) and also thank Shenyang Yuanjie Optics Technology Co., ltd, for LCM characterizations.

Author contributions

All authors contributed to the study conception and design. Material preparation, data collection, and analysis were performed by XJ, RA, WZ, and YX. The researches were sponsored by CW, FG, and XJ. The first draft of the manuscript was written by XJ and all authors commented on previous versions of the manuscript. All authors read and approved the final manuscript.

Data Availability

The datasets generated during and/or analyzed during the current study are available from the corresponding author on reasonable request.

Declarations

Conflict of interest The authors have no relevant financial or non-financial interests to disclose.

Supplementary Information: The online version contains supplementary material available at https://doi.org/10.1007/s10854-022-09757-7.

References

1. M. Abtew, G. Selvaduray, Lead-free Solders in Microelectronics. Mater. Sci. Eng. R **27**, 95–141 (2000). https://doi.org/10.1016/S0927-796X(00)00010-3
2. T.K. Lee, T.R. Bieler, C.U. Kim, H. Ma, *Fundamentals of lead-free Solder Interconnect Technology* (Springer, New York, 2015)
3. B. Wu, Y.-H. Yang, B. Han, J. Schumacher, Measurement of anisotropic coefficients of thermal expansion of SAC305 solder using surface strains of single grain with arbitrary orientation. Acta Mater. **156**, 196–204 (2018). https://doi.org/10.1016/j.actamat.2018.06.032
4. A.U. Telang, T.R. Bieler, A. Zamiri, F. Pourboghrat, Incremental recrystallization/grain growth driven by elastic strain energy release in a thermomechanically fatigued lead-free solder joint. Acta Mater. **55**, 2265–2277 (2007). https://doi.org/10.1016/j.actamat.2006.11.023
5. M.L. Huang, J.F. Zhao, Z.J. Zhang, N. Zhao, Role of diffusion anisotropy in β-Sn in microstructural evolution of Sn-3.0Ag-0.5Cu flip chip bumps undergoing electromigration. Acta Mater. **100**, 98–106 (2015). https://doi.org/10.1016/j.actamat.2015.08.037
6. Z.Y. Liang, S.S. Xiang, G.M. Pharr, Effects of crystal orientation on the indentation creep of β–tin. J. Mater. Res. **36**, 2434–2443 (2021). https://doi.org/10.1557/s43578-021-00165-x

7. J. Han, F. Guo, J.P. Liu, Effects of anisotropy of tin on grain orientation evolution in Pb-free solder joints under thermo-mechanical stress. J. Mater. Sci: Mater. Electron. **28**, 6572–6582 (2017). https://doi.org/10.1007/s10854-017-6347-2
8. S.H. Yang, Y.H. Tian, C.Q. Wang, Investigation on Sn grain number and crystal orientation in the Sn-Ag-Cu/Cu solder joints of different sizes. J. Mater. Electron. **21**, 1174–1180 (2010). https://doi.org/10.1007/s10854-009-0042-x
9. C.Y. Cai, J.F. Xu, H.Y. Wang, S.B. Park, A comparative study of thermal fatigue life of eutectic Sn-Bi, hybrid Sn-Bi/SAC and SAC solder alloy BGAs. Microelectron. Reliab. **119**, 114065 (2021). https://doi.org/10.1016/j.microrel.2021.114065
10. S. Wei, H.C. Ma, J.Q. Chen, J.D. Guo, Extreme anisotropy of electromigration: Nickel in single-crystal tin. J. Alloys Compd. **687**, 999–1003 (2016). https://doi.org/10.1016/j.jallcom.2016.06.253
11. Q. Jiang, A. Dasgupta, Anisotropic steady-state creep behavior of single-crystal β-Sn: a continuum constitutive model based on crystal viscoplasticity. Int. J. Plast. **140**, 102975 (2021). https://doi.org/10.1016/j.ijplas.2021.102975
12. X.L. Ji, R. An, W. Zhou, Y. Zhong, F. Guo, C.Q. Wang, Revealing the ductile-to-brittle transition mechanism in polycrystalline body-centered tetragonal tin (sn) for cryogenic electronics. J. Alloys Compd. **903**, 163948 (2022). https://doi.org/10.1016/j.jallcom.2022.163948
13. X.L. Ji, R. An, F. Ma, J.W. Hu, C.Q. Wang, Unique buoyancy-force-based kinetics determination of beta to alpha phase transformation in bulk tin plates. Mater. Des. **190**, 108500 (2020). https://doi.org/10.1016/j.matdes.2020.108550
14. M.S. Grinolds, S. Hong, P. Maletinsky, L. Luan, M.D. Lukin, R.L. Walsworth, A. Yacoby, Nanoscale magnetic imaging of a single electron spin under ambient conditions. Nat. Phys. **9**, 215–219 (2013). https://doi.org/10.1038/nphys2543
15. A. Kitamura, T. Matthews, R. Contreras, D. Routledge, T.-K. Lee, Impact of cryogenic temperature environment on single solder joint mechanical shear stability. J. Electron. Mater. **50**, 723–734 (2021). https://doi.org/10.1007/s11664-020-08456-5
16. X.L. Ji, Q. An, Y.P. Xia, R. An, R. Zheng, C.Q. Wang, Maximum shear stress controlled uniaxial tensile deformation and fracture mechanisms and constitutive relations of Sn–Pb eutectic alloy at cryogenic temperatures. Mater. Sci. Eng. A **819**, 141523 (2021). https://doi.org/10.1016/j.msea.2021.141523
17. Q. Jiang, A. Deshpande, A. Dasgupta, Multi-scale crystal viscoplasticity approach for estimating anisotropic steady-state creep properties of single-crystal SnAgCu alloys. Int. J. Plast. **153**, 103271 (2022). https://doi.org/10.1016/j.ijplas.2022.103271
18. Z. Ma, S. Belyakov, K. Sweatman, T. Nishimura, T. Nishimura, C. Gourlay, Harnessing heterogeneous nucleation to control tin orientations in electronic interconnections. Nat. Commun. **8**, 1916 (2017). https://doi.org/10.1038/s41467-017-01727-6
19. T.Y. Chen, L.Z. Tan, Z.Z. Lu, H.X. Xu, The effect of grain orientation on nanoindentation behavior of model austenitic alloy Fe-20Cr-25Ni. Acta Mater. **138**, 83–91 (2017). https://doi.org/10.1016/j.actamat.2017.07.028
20. C. Zambaldi, D. Raabe, Plastic anisotropy of γ-TiAl revealed by axisymmetric indentation. Acta Mater. **58**, 3516–3530 (2010). https://doi.org/10.1016/j.actamat.2010.02.025
21. G. Muthupandi, K.R. Lim, Y.S. Na, J. Park, D.Y. Lee, H.J. Kim, S. Park, Y.S. Choi, Pile-up and sink-in nanoindentation behaviors in AlCoCrFeNi multi-phase high entropy alloy. Mater. Sci. Eng. A **696**, 146–154 (2017). https://doi.org/10.1016/j.msea.2017.04.045
22. A.C. Fischer-Cripps, Nanoindentation, third ed. Springer, New York, 2011
23. Tabor, *The Hardness of Metals*, first edn. (Clarendon Press, Oxford, 1951)
24. O. Casals, J. Alcalá, The duality in mechanical property extractions from Vickers and Berkovich instrumented indentation experiments. Acta Mater. **53**, 3545–3561 (2005). https://doi.org/10.1016/j.actamat.2005.03.051
25. J. Alcalá, A.C. Barone, M. Anglada, The influence of plastic hardening on surface deformation modes around Vickers and spherical indents. Acta Mater. **48**, 3451–3464 (2000). https://doi.org/10.1016/S1359-6454(00)00140-3
26. Dewei, Han, *Handbook of Metal Hardness Measurement*, 1st edn. (Central South University Press, Changsha, 2003)
27. Y. Zhou, *Material Analysis Methods*, 3rd edn. (China Machine, Beijing, 2011)
28. A. Bolshakov, G.M. Pharr, Mechanical property evaluation through sharp indentations in elastoplastic and fully plastic contact regimes. J. Mater. Res. **13**, 1049–1058 (1998). https://doi.org/10.1557/JMR.2003.0234
29. H.J. Zhou, M.Z. Huang, *Strength Metall. Mater.*, 1st edn. (Science Press, Beijing, 1989)
30. P. Peralta, R. Ledoux, R. Dickerson, M. Hakik, P. Dickerson, Characterization of surface deformation around vickers indents in monocrystalline materials. Metall. Mater. Trans. A **35A**, 2247–2255 (2004). https://doi.org/10.1007/s11661-006-0204-x
31. B. Wang, L. Deng, N. Guo, Z. Xu, Q. Li, EBSD analysis of {10–12} twinning activity in Mg–3Al–1Zn alloy during compression. Mater. Charact. **98**, 180–185 (2014). https://doi.org/10.1016/j.matchar.2014.10.015

32. K.A. Nibur, D.F. Bahr, Identifying slip systems around indentations in FCC metals. Scripta Mater. **49**, 1055–1060 (2003). https://doi.org/10.1016/j.scriptamat.2003.08.021
33. D. Hull, D.J. Bacon, *Introduction to Dislocations*, 5th edn. (Elsevier, London, 2011)
34. J.P. Hirth, J. Lothe, Theory of dislocations, second eds., Wiley, New York, 1982
35. C.S. Kaira, S.S. Singh, A. Kirubanandham, N. Chawla, Microscale deformation behavior of bicrystal boundaries in pure tin (sn) using micropillar compression. Acta Mater. **120**, 56–67 (2016). https://doi.org/10.1016/j.actamat.2016.08.030
36. Y. Kinoshita, H. Matsushima, N. Ohno, Predicting active slip systems in β-Sn from ideal shear resistance. Model. Simul. Mater. Sci. Eng. **20**, 035003 (2012). https://doi.org/10.1088/0965-0393/20/3/035003
37. X. Wang, Y. Han, X. Su, G. Huang, W. Lu, The formation of $\{10\bar{1}2\}$ deformation twin in hybrid tib-tic reinforced titanium matrix composites. Metall. Mater. Trans. A **52**, 350–363 (2021). https://doi.org/10.1007/s11661-020-06067-7
38. S. Gollapudi, M.A. Azeem, A. Tewari, U. Ramamurty, Orientation dependence of the indentation impression morphology in a mg alloy. Scripta Mater. **64**, 189–192 (2011). https://doi.org/10.1016/j.scriptamat.2010.09.041